Thermal Degradation Kinetics of Calcium-Enriched Bio-oil

Yang Xulai, Zhang Jian, and Zhu Xifeng
Key Laboratory for Biomass Clean Energy of Anhui Province, University of Science and Technology of China, Hefei, 230026, P.R. China

DOI 10.1002/aic.11507
Published online May 22, 2008 in Wiley InterScience (www.interscience.wiley.com).

The thermal decomposition of calcium-enriched bio-oil (CEB) was studied in air by thermogravimetric experiments. The characteristics, to a great extent, are quite similar to that of calcium acetate (CA). The decomposition processes can be divided into four stages: the loss of volatile materials, devolatilization and degradation of pyrolytic lignin, decomposition of organic calcium salts and residual carbon, decomposition of $CaCO_3$ to CaO. The activation energy values are lower than that of CA at the corresponding decomposition stages. The $CaCO_3$ from amorphous CEBs exhibits the higher calcination rate than that from CA. The actual mechanisms of the second and the third stages obey the nucleation and growth model (A1), with integral form of $F(\alpha) = -ln(1 - \alpha)$. The high-porosity of calcined CEBs should be the further evidence of the mechanism. Correspondingly, the mechanism of the fourth stage obeys three-dimensional (3-D) phase boundary reaction (R3) mechanism with integral form of $F(\alpha) = 1-(1 - \alpha)^{1/3}$. © 2008 American Institute of Chemical Engineers *AIChE J,* 54: 1945–1953, 2008
Keywords: bio-oil, thermogravimetric analysis, kinetics, reaction mechanism

Introduction

There is an increasing concern with environmental problems associated with the rising emissions of CO_2, NO_x and SO_x resulting from the use of fossil fuels. Calcium-containing materials, mostly based on calcium carbonate and calcium hydroxide, are the most commonly used adsorbents for *in situ* removal of SO_x, and consider being a simpler and cheaper method to control SO_x emission in coal combustions at the power plant site.[1,2]

Recently, some studies indicated that CaO particles derived from organic calcium salts, such as calcium acetate (CA) and calcium magnesium acetate (CMA) demonstrated the unique properties with a large internal surface area for *in situ* removal of SO_x.[3,4] However, producing the organically bonded calcium by the reactions of lime or calcium hydroxide with the conventional acetic acid makes these adsorbents more expensive than the natural ones and commercial uses impossible. Recently, low-cost bio-oil, which is usually used as renewable liquid fuel, was modified by adding lime in order to produce calcium-enriched bio-oil that contained the organically bonded calcium to be used as an absorbent.[5,6] The bio-oil can be obtained easily by rapid pyrolysis of any kind of biomass in the absence of oxygen, whereby subsequent condensation of the product vapors yields 70 wt % bio-oil, which contain about 10 wt % acidic content (the major acids found in it are acetate acid and formic acid).[7–9]

For the reactions of sulfur dioxide with basic solid oxides, a suitable surface area and high porosity of absorbents are beneficial for the reactions. Moreover, we consider that if the precursors of absorbents are converted easily to target basic solid oxides, the oxides can react with sulfur dioxide for longer time to achieve a higher utilization of calcium. Consequently, we investigated the experimental results of the thermal decomposition of CEBs including the thermal decomposition path and detailed kinetics of the reactions. To compare the thermal behavior of CEBs with other organic calcium

Correspondence concerning this article should be addressed to X. Zhu at xfzhu@ustc.edu.cn.

Table 1. Algebraic Expressions for $f(\alpha)$ and $F(\alpha)$ for the Most Frequently used Mechanisms of Solid-State Processes

No.	Symbol	Mechanism	$f(\alpha)$	$F(\alpha)$
1	D1	1-Dimensional diffusion	$1/(2\alpha)$	α^2
2	D2	2-Dimensional diffusion (Valensi Eq.)	$[-\ln(1-\alpha)]^{-1}$	$\alpha+(1-\alpha)\ln(1-\alpha)$
3	D3	3-Dimensional diffusion (sphere, Jander Eq.)	$1.5[(1-\alpha)^{-1/3}-1]^{-1}$	$(1-2\alpha/3)-(1-\alpha)^{2/3}$
4	D3	3-Dimensional diffusion (cylinder, GB Eq.)	$1.5(1-\alpha)^{2/3}[1-(1-\alpha)^{1/3}]^{-1}$	$[1-(1-\alpha)^{1/3}]^2$
5	A1	Nucleation and nuclei growth (Avrami-Erofeev Eq., n=1)	$1-\alpha$	$-\ln(1-\alpha)$
6	A1.5	Nucleation and nuclei growth (Avrami-Erofeev Eq., n=1.5)	$3/2(1-\alpha)[-\ln(1-\alpha)]^{1/3}$	$[-\ln(1-\alpha)]^{2/3}$
7	A2	Nucleation and nuclei growth (Avrami-Erofeev Eq., n=2)	$2(1-\alpha)[-\ln(1-\alpha)]^{1/2}$	$[-\ln(1-\alpha)]^{1/2}$
8	A3	Nucleation and nuclei growth (Avrami-Erofeev Eq., n=3)	$3(1-\alpha)[-\ln(1-\alpha)]^{2/3}$	$[-\ln(1-\alpha)]^{1/3}$
9	P1	Exponential nucleation (Mample Eq.)	1	α
10	P2	Exponential nucleation (Mample Eq.)	$2\alpha^{1/2}$	$\alpha^{1/2}$
11	P3	Exponential nucleation (Mample Eq.)	$3\alpha^{2/3}$	$\alpha^{1/3}$
12	P4	Exponential nucleation (Mample Eq.)	$4\alpha^{3/4}$	$\alpha^{1/4}$
13	C1.5	Power law (n=1.5)	$(1-\alpha)^{1.5}$	$(1-\alpha)^{-1/2}$
14	C2	Power law (n=2)	$(1-\alpha)^2$	$(1-\alpha)^{-1}$
15	R2	2-Dimensional phase boundary reaction	$2(1-\alpha)^{1/2}$	$1-(1-\alpha)^{1/2}$
16	R3	3-Dimensional phase boundary reaction	$3(1-\alpha)^{2/3}$	$1-(1-\alpha)^{1/3}$

salts in the same condition, the experiment was also carried out using calcium acetate.

Thermogravimetric analysis (TGA) is one of the most common techniques used to investigate thermal events and kinetics during pyrolysis of solid raw materials.[5,10–12] In this method, the change of a sample mass is monitored against time or temperature at a specific heating rate. The kinetics of the thermal events can be determined by the application of the Arrhenius equation corresponding to the separate slopes of constant mass degradation. However, the determination of the kinetic parameters for the degradation from the TGA data strongly depends on the method of calculation.[13] In this study, the thermal decomposition experiments were carried out using a DTG-60H thermogravimetric analyzer under air-flow. The thermal degradation kinetic parameters, activation energy (E_a), and pre-exponential factor (A), were evaluated by using two well-known integral methods, Coats-Redfern and Doyle methods, which have been found to be the most versatile integral approach method in calculating the kinetic parameters for the degradation process in nonisothermal kinetic analysis, and can be used without prior knowledge of reaction mechanism.[14–16] Additionally, Coats-Redfern method was used because it renders the degradation parameters, such as E_a, A, and possible reaction mechanisms.[10]

Kinetic Theoretical Background

In general, the decomposition of solid polymer can be associated with the reactions, which may be represented by the processes of

$$\text{A (solid)} \rightarrow B \text{ (solid)} + C \text{ (gas)} \tag{1}$$

where A is the initial, B is the residue, and C is the gas. For thermogravimetric analysis, the degree of decomposition (conversion) can be calculated as follows

$$\alpha = (w_0 - w)/(w_0 - w_c) \tag{2}$$

A typical model for a kinetic process can be expressed as

$$d\alpha/dt = k \cdot f(\alpha) \tag{3}$$

where $d\alpha/dt$ is the decomposition rate, k is the decomposition rate constant, and $f(\alpha)$ is the differential expression of a kinetic model function, which depends on the particular decomposition mechanism. The temperature dependence of the rate constant k may be described by the Arrhenius expression

$$k = A\exp(-E_a/RT) \tag{4}$$

where A is the pre-exponential factor (min^{-1}), assumed to be independent of temperature.

A combination of Eqs. 3 and 4 leads to

$$d\alpha/dt = A\exp(-E_a/RT)f(\alpha) \tag{5}$$

If the sample temperature is changed by a controlled and constant heating rate β ($\beta = dT/dt$), Eq. 5 can be changed to

$$d\alpha/dT = \frac{A}{\beta}\exp(-E_a/RT)f(\alpha) \tag{6}$$

Therefore, Eq. 6 is the fundamental relation to determine kinetic parameters on the basis of TG data. Through variable separation and integration of Eq. 6 from an initial temperature T_0, corresponding to a degree of conversion α_0, to the peak temperature, T_p, where $\alpha = \alpha_p$, gives

$$F(\alpha) = \int_{\alpha_0}^{\alpha_p} d\alpha/f(\alpha) = \frac{A}{\beta}\int_{T_0}^{T_p} \exp\left(-\frac{E}{RT}\right)dT \tag{7}$$

where $F(\alpha)$ is the integral function of conversion.

The Coats-Redfern method used an asymptotic approximation for the resolution of Eq. 7 at different conversion values.[15] A natural logarithmic form can be obtained

$$\ln\frac{F(\alpha)}{T^2} = \ln\frac{AR}{\beta E_a}\left(1-\frac{2RT}{E_a}\right) - \frac{E_a}{RT} \tag{8}$$

Since in general $2RT/E_a \ll 1$, and it exhibits a small variation with T, for practical considerations it is assumed that the term $(1-2\frac{RT}{E_a})$ is approximately constant and equal to unity. According to the different degradation processes, the theroretical functions were listed in Table 1. These functions were satisfactorily used in the known method for the estimation of the most probable reaction mechanisms from dynamic TG curves.[17–19] Thus, for a given form of $F(\alpha)$, the plot of $\ln[F(\alpha)/T^2]$ vs. $1/T$ gives a straight line whose slope and intercept allow an estimation of the values of the activation energy and pre-exponential factor, respectively.

Table 2. The Physical Characteristics of Bio-Oil used in this Study

Water content (wt.%)	LHV (MJ/kg)	pH	Elemental analysis (wt.%)			
			C	H	O	N
28	16.5	3.2	39.92	8.18	51.07	0.61

For comparison, Doyle method expressed as Eq. 9 was also used in the study to determine apparent activation energy[16]

$$\ln F(\alpha) = \ln \frac{AE_a}{\beta R} - 5.3305 - 1.052 \frac{E_a}{R} \cdot \frac{1}{T} \qquad (9)$$

Experimental

Production and characteristics of bio-oil

The bio-oil derived from rice husk was produced by fast pyrolysis operation in an autothermal fluidized-bed reactor with capacity of 120 kg/h in our laboratory. The characteristics of the pyrolysis reactor have been described elsewhere,[20] so only the essential information was provided here. Table 2 opened up the physical property of bio-oil used in the study. The organic acids mainly comprising acetic acid account for about 6.97 wt % of whole bio-oil. Esters and aldehydes which are potential sources of acids (via hydrolyzed and oxidized) make up about 1.15 wt % of the whole bio-oil.

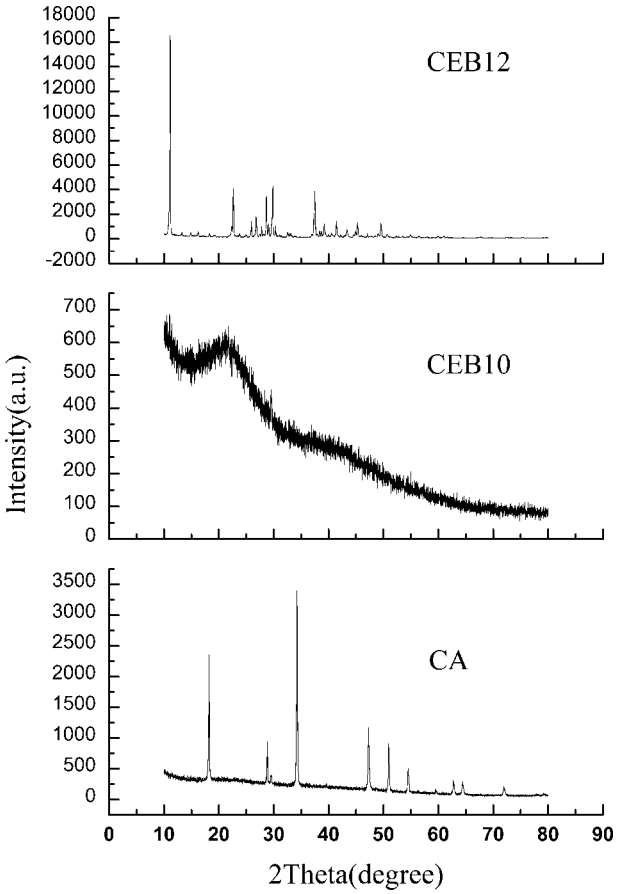

Figure 1. XRD patterns of specimens.

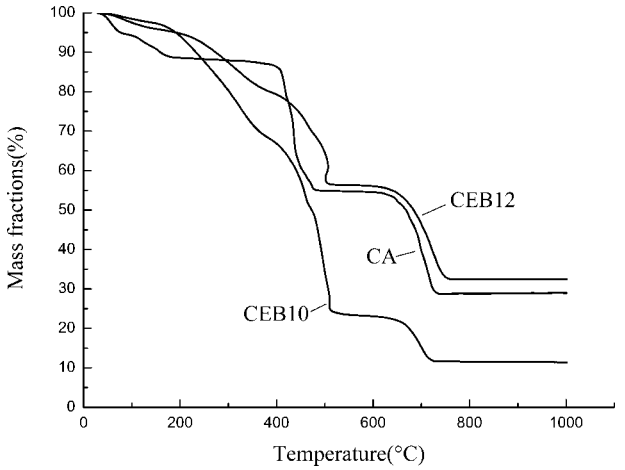

Figure 2. TG curves of specimens.

Apparatus and Procedure

Calcium hydroxide of analytical pure used in the study was produced by China National Medicines Corporation, Ltd., which were added into the bio-oil under stirring vigorously, then ultrasonically at 60°C for 20 min to adjust the pH to an alkaline level sufficient to hydrolyze the esters, caused at least partial oxidation of the formaldehyde. The pH is preferably above 7, but preferably sufficiently low as to avoid residual unreacted calcium hydroxide in the calcium salts. The pH of 10 and 12 were practiced in the study, whereas the pH of bio-oil was about 3.2. The synthesized samples were named CEBX, where X is the pH value of synthesis medium. Then CEBs were evaporated *in vacuo* to partly remove the majority of the water and volatile materials, and then semisolid CEBs were obtained. The said CEBs were dried at 110°C, and powdered to particles with a mesh size of a 120 through mechanical sieving for study.

The dried CEBs obtained in pH of 10, 12, respectively, were analyzed by XRD analysis on a Rigaku (Japan) D/max-γA X-ray diffractometer to investigate the chemical species and mode of occurrence of calcium within the CEBs. The XRD analysis conditions were the same as that used for calcium acetate compares to CEBs. The decomposition experiments were carried out using a thermogravimetric analysis (TGA) system on a DTG-60H detector. The samples were evenly and loosely distributed in an open sample pan of 6.4 mm dia. and 3.2 mm deep, with an initial sample amount of 8 mg. Due to different bulk density, the depth of the sample layer filled in the pan was about 1-2 mm. The temperature change was controlled from room-temperature to 1,000°C at a heating rate of 10 °C/min, and kept at the temperature for 30 min for the purpose of full calcination to calcium oxide. The small amount of sample and the slow heating rate ensures that the heat-transfer limitations can be ignored.[11,21] An airstream was continuously passed into the furnace at a flow rate of 50 mL/min at atmospheric pressure during devolatilization, and to carry away the decomposition products from the reaction zones. The specific surface area of calcined samples was measured by N_2 physisorption at 77 K in a Micromeritics ASAP 2020 M+C analyzer, and using the BET multipoint method over a P/P_0 range of 0–1.0.

Table 3. Fractions of Volatile Products Released Along the Four Temperature Zones Defined by TGA

CA		CEB10		CEB12	
Temperature Zones (°C)	Mass Loss (wt.%)	Temperature Zones (°C)	Mass Loss (wt.%)	Temperature Zones (°C)	Mass Loss (wt.%)
28–196	11.438	28–133	2.306	29–161	4.312
–	–	135–390	30.198	163–409	16.965
363–483	32.298	395–555	44.061	410–531	22.342
607–744	25.666	556–726	11.795	533–756	23.927

Data Processing

An initial sample amount of all specimens was about 8 mg for TGA. The TG and derivative thermogravimetric (DTG) curves obtained from TGA runs were carefully smoothed at a smoothing region width of 0.2°C by using least-squares smoothing method, and analyzed by using OriginPro 7.5. Activation energy values were calculated with a specially designed program in MS Excel, which took specific TG and DTG data from the OriginPro Analysis software. To verify the reproducibility of obtained mass loss curves, two sample runs were performed under the same experimental conditions for each kind of samples first. The approximate overlapping of two weight loss curves from two separate test runs was considered as reasonable agreement; otherwise, another two runs were performed then to determine which one should be chosen.

Result and Discussion

Physicochemical properties of CEBs

The content of calcium hydroxide in CEBs affects severely the characteristics of CEBs. CEB10 was homogeneous liquid before dried at 110°C, and could be sprayed into combustors used as absorbents, but CEB12 exhibited the rapid phase separation during the synthesis process, which was impossible to use as liquid form. The chemical species and mode of occurrence of calcium within CEBs were analyzed by XRD, which were shown in Figure 1. The broad X-ray diffraction pattern of CEB10, which was typical for amorphous solids, confirmed the absence of any ordered crystalline structure, and did not match the peaks of pure calcium acetate or raw calcium hydroxide at all. This fact indicated that calcium hydroxide in CEB10 was reacted with some components in bio-oil to form amorphous organic calcium salts. For CEB12, all of its peaks match those of the raw calcium hydroxide. This result should be due to the impurity caused during the reaction, which may be because of the raw material calcium hydroxide having a higher crystalline degree than the organically bonded calcium. These results imply the formation of an amorphous structure of organically bonded calcium within the CEBs.

The TG results were shown in Figure 2. It can be found that decomposition curves of CEBs were similar with that of CA, which mainly consisted of four steps, also as can be seen from Table 3. For CEBs, as the sample temperature is raised, mass loss is continuous until $CaCO_3$ particles were converted into CaO completely. The DTG curves of specimens were listed in Figure 3. The initial decomposition step of CEBs was due to the loss of water (free and hydration) and volatile materials. Devolatilization and degradation of unreacted organic materials (probably pyrolytic lignin) occurred in the second mass loss step. Because almost all of the organic materials in CA were in the form of organic calcium salts, the mass loss of CA in the temperature zone was not detected obviously. The third step and the quick decomposition step of in CEBs took place initiating at about 430°C, and nearly the greatest mass loss during the decomposition of organic calcium salts to $CaCO_3$ took place at this stage. Calcium content of CEB10 was much lower than that of CA, but the mass loss was higher at this stage. This fact indicated the mass loss was not only due to the decomposition of organic calcium salts, but also due to some progress of pyrolysis, and/or gasification of the carbon and organic

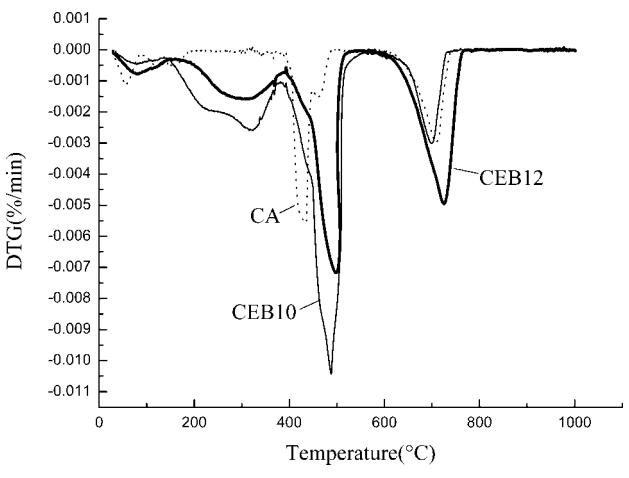

Figure 3. DTG curves of specimens.

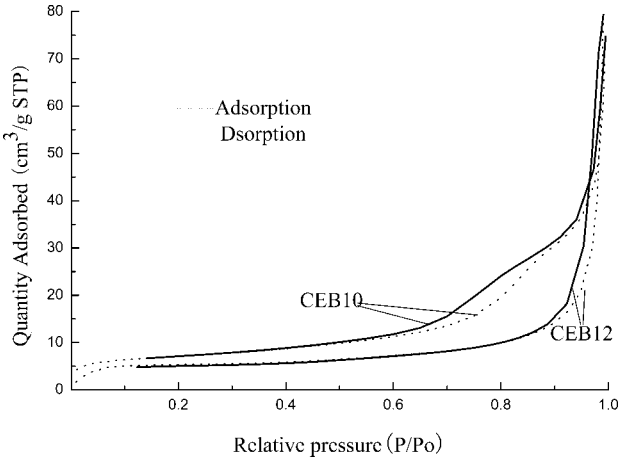

Figure 4. Nitrogen adsorption-desorption isotherms for CEBs calcined at 1,000°C

Table 4. Surface Areas and Porosities of the Specimens Calcined at 1,000°C

	CA	CEB10	CEB12
Surface area ($m^2.g^{-1}$)	30.0	17.6	15.4
Porosity (%)	76.4	86.3	83.4

compounds remaining in the adsorbents. The decomposition rates of CEBs at this temperature zone were lower than that of CA. The fourth and final decomposition step took place starting at about 550°C, and the weight loss was mainly due to the decomposition of $CaCO_3$ to CaO. At this stage, calcination rates of $CaCO_3$ derived from CEBs was a little faster than in the case of CA, and the termination decomposition temperatures of $CaCO_3$ were 726°C for CEB10, 744°C for CA and 756°C for CEB12.

The nitrogen adsorption-desorption isotherms of CEBs after calcination at 1,000°C were presented in Figure 4. The isotherms of particles from CEBs could be classified as being of type H3 according to IUPAC classification, which were characteristic of mesoporous material.[22] Hysteresis is usually attributed to different size of pore mouth and pore body.[23] The observed hysteresis loops presented in the range of 0.55–0.9 P/P_0 for particles from CEB8 and CEB10, but approached $P/P_0 = 1$ for particles from CEB12. As can be seen from Table 4, the porosities of calcined CEBs were a little higher than that of calcined CA, but their BET surface areas were a lot lower. This suggests that CA-derived particles contain a larger number of finer pores which contribute the most to heterogeneous sulfation reactions, if of course pore plugging is not widespread. Actually, pore plugging is unavoidable in utility boilers sulfation. Therefore, large porosity and suitable surface area of particles from CEBs should be beneficial for heterogeneous sulfation reactions.

Degradation kinetic analysis

The probable thermal degradation kinetic mechanisms were evaluated from a TGA curve at a constant heating rate (β) by Coats-Redfern method and Doyle method. In this study, E_a and A were not analyzed while the correlation coefficient (r) was smaller than 0.98. The fitting results of Coats-Redfern equation and Doyle equation were opened up in Table 5.

The most probable mechanism was chosen where two values of E_a and A calculated by two methods were very close to each other with the best linearity, corresponding to the maximum correlation coefficient at the stage of $20 \leq \frac{E_a}{RT} \leq 60$. Due to the approximation techniques used in the integration, the kinetic parameters are more precise than those with the other methods.[13] The values of E_a and A calculated by Coats-Redfern equation were chosen to be optimal results. As can be seen from Table 5, the correlation of mechanism A1 (nucleation and nuclei growth, n = 1) was better for the third stage of CA thermal decomposition, or the second and the third stages of CEB10 and CEB12 decomposition. At these stages the thermal decomposition often accompanied by melting (or softening) can be controlled by the process of formation of a gas phase inside the specimens, and by nucleation and nucleus growth in a heterogeneous medium.[24] The high-porosity of the calcined CEBs or CA could be the further evidence of the A1 mechanism. The high-porosity of CEB-derived particles are due to the facts that the gases that are formed during decomposition of the organic salts, and the vapors formed from the violent boiling of the molten materials, or of the droplets lead to the formation of bubbles inside the decomposing structures, then the bubbles can coalesce under some conditions into a single bubble, and while this happens, the resulting particles have the form of cenospheres surrounded by a thin shell of CaO perforated with a number of blow holes through which the decomposition gases escaped. The kinetic parameters, E_a and A, at the second stages of CEB10 and CEB12 resulted to be 15.748 kJ/mol and 1.35E+03 min^{-1}, 20.044 kJ/mol and 3.91E+03 min^{-1}, respectively. The two activation energies were in good agreement with literature data of lignin decomposition.[25,26] This result confirmed that devolatilization and degradation of pyrolytic lignin in the CEBs occurred in the second mass loss step.

The E_a in the third decomposition stages of CA, CEB10 and CEB12 were 95.487 kJ/mol, 67.04 kJ/mol and 67.342 kJ/mol, respectively. The E_a of CA in the stage was in good agreement with literature data.[27,28] Obviously, the E_a of CEBs at the stage was lower than that in the case of CA. This fact should be the further evidence of that the mass loss at this stage was not only due to the decomposition of organic calcium salts, but also due to some progress of pyrolysis, and/or gasification of the carbon and organic compounds remaining in CEBs. After this stage, porous calcium carbonate derived from CEBs was formed because of the releasing of gas phase formed inside the specimens. However, CA-derived particles exhibited a much higher decomposition rate than particles from CEBs at this stage. In this study, we have no idea how to understand why the particles from CEBs had lower activated energy, but higher decomposition temperature at this decomposition stage.

Table 5 also showed that the mechanisms of the fourth step in degradation process of all specimens except CEB12 were in better agreement with R3(3-D phase boundary reaction) mechanism, assuming an isotropic shrinkage of a cubic or spherical particle with a constant rate of interface

Table 5. Kinetic Parameters Calculated by Coats-Redfern Method and Doyle Method

			Coats-Redfern Method			Doyle Method		
Samples	Decomposition Stages	Reaction Mechanisms	E_a/kJ·mol^{-1}	A/min	r	E_a/kJ·mol^{-1}	A/min	r
CA	The third stage	A1	95.487	3.16E+09	0.99038	95.522	3.46E+09	0.99133
	The fourth stage	R3	137.034	5.26E+09	0.99861	136.648	3.62E+09	0.99876
CEB10	The second stage	A1	15.748	1.35E+03	0.9941	18.633	3.66E+03	0.99659
	The third stage	A1	67.039	6.83E+06	0.98771	68.667	1.53E+07	0.98954
	The fourth stage	R3	116.297	3.55E+08	0.99879	116.877	3.34E+08	0.99899
CEB12	The second stage	A1	20.043	3.91E+03	0.99794	22.687	6.80E+03	0.99878
	The third stage	A1	67.341	6.86E+06	0.98242	69.011	1.54E+07	0.98501
	The fourth stage	A1	112.833	2.10E+08	0.99983	113.592	2.10E+08	0.99987

advancement. The mechanism gives a good fit for previous experiment data of the decomposition of calcium carbonate in previous literature.[29] The values of E_a at this stage resulted to be 137.035 kJ/mol, 116.297 kJ/mol and 112.834 kJ/mol for CA, CEB10 and CEB12, respectively, which were far lower than that of calcite decomposition (about 163–250 kJ/mol[1,30]). Therefore, it is easy to understand that CEB10 exhibits a little higher calcination rate than CA at this decomposition stage. The result might be due to the formation of nanoparticles with higher surface free energy[29] in degradation processes of amorphous CEBs.

In addition, it was found that a high pH of CEB synthetic medium was followed with a high content of residual unreacted calcium hydroxide in CEBs. CEB12 exhibited a lower decomposition starting temperature, and lower activation energy than that of CEB10 and CA at the fourth stage, but a little lower calcination rate. The result should be because of much residual unreacted calcium hydroxide existed in CEB12. However, the high-porosity of the CEB-derived $CaCO_3$ makes it exhibit a much higher calcination rate than particles of limestones and calcites.[5,6]

Conclusion

The content of calcium hydroxide in CEBs affects severely the characteristics of CEBs. CEB10 was homogeneous liquid before dried at 110°C, and CEB12 exhibited the rapid phase separation during the synthesis process. Thermal degradation process of CEBs might be comprised of four stages. The first mass loss stage was due to the loss of water and/or small volatiles. The kinetic parameters were not investigated in this study for this stage. The second stage could be considered to be the pyrolytic lignin decomposition. Organic calcium salts and residual carbon were decomposed at the third stage. The CEB-derived $CaCO_3$ particles were degraded at the last stage for the formation of CaO particles. The CaO particles were mesoporous materials of very high-porosity, more than 80% and moderate surface area.

The kinetic analysis of last three steps of the four-step decomposition of CEBs was carried out using the Coats-Redfern and Doyle methods. The actual mechanisms of the second and the third stages obeyed nucleation and growth model, Avrami-Erofeev function (A1), with integral form $F(\alpha) = -\ln(1 - \alpha)$, as well as the fourth stage of CEB12 decomposition. Correspondingly, the mechanisms of the fourth stages of CA and CEB10 obeyed 3-D phase boundary reaction (R3) mechanism, with integral form $F(\alpha) = 1-(1 - \alpha)^{1/3}$. The apparent activation energies E_a of CEBs thermal decomposition were a little lower than that of CA at all decomposition stages. The CaO particles obtained from amorphous CEBs generated more easily than that from CA. This advanced adsorbent used in the fossil fuel combustors may improve the utilization of calcium in the process of desulfurization.

Acknowledgments

The authors gratefully acknowledge financial support from National Natural Science Foundation of China (NO. 50576091), Chinese Academy of Sciences Innovation Program (No. KGCX2-YW-306-4) and Tackling Key Program of Science and Technology of Anhui Province (NO. 06013109B).

Notation

w_0 = initial weight of the sample, mg
w_c = final weight of the sample, mg
w = actual weight of the sample, mg
β = heating rate, °C/min
α = degree of decomposition, reaction ratio
k = decomposition rate constant
T = absolute temperature, K
E_a = activation energy, kJ/mol
$f(\alpha)$ = differential expression of a kinetic model function
$F(\alpha)$ = integral function of conversion.
r = correlation coefficient
R = gas constant, 8.314 J/mol·K
A = pre-exponential factor, min^{-1}

Literature Cited

1. Han DH, Sohn HY. Calcined calcium magnesium acetate as a superior SO_2 sorbent: I. thermal decomposition. *AIChE J*. 2002;42(18): 2971–2977.
2. Wei SH, Mahuli SK, Agnihotri R, Fan LS. High surface area calcium carbonate: pore structural properties and sulfation characteristics. *Ind Eng Chem Res*. 1997;36:2141–2148.
3. Wu Shengji, Naomi Sumie, Su Caili, Sasaoka Eiji. Preparation of macroporous lime from natural lime by swelling method with water and acetic acid mixture for removal of sulfur dioxide at high-temperature. *Ind Eng Chem Res*. 2002;41:1352–1356.
4. Patsias AA, Nimmo W, Gibbs BM, Williams PT. Calcium-based sorbents for simultaneous NOx/SOx reduction in a down-fired furnace. *Fuel*. 2005;84:1864–1873.
5. Sotirchos Stratis V, Smith Adam R. Experimental investigation of the decomposition and calcination of calcium-enriched bio-oil. *Ind Eng Chem Res*. 2003;42:2245–2255.
6. Sotirchos Stratis V, Smith Adam R. Performance of porous CaO obtained from the decomposition of calcium-enriched bio-oil as sorbent for SO_2 and H_2S removal. *Ind Eng Chem Res*. 2004;43:1340–1348.
7. Carmen Branca, Paola Giudicianni, Colomba Di Blasi. GC/MS Characterization of liquids generated from low-temperature pyrolysis of wood. *Ind Eng Chem Res*. 2003;42:3190–3202.
8. Diebold JP. A review of the chemical and physical mechanisms of the storage stability of fast pyrolysis bio-oils. Report No. NREL/SR-570–27613, National Renewable Energy Laboratory, Golden, CO; 2000.
9. Mohan D, Pittman CU, Steele PH. Pyrolysis of wood/biomass for bio-oil: A critical review. *Energy Fuels*. 2006;20(3):848–889.
10. Sunan Tiptipakorn, Siriporn Damrongsakkul, Shinji Ando, Kasinee Hemvichian, Sarawut Rimdusit. Thermal degradation behaviors of polybenzoxazine and silicon-containing polyimide blends. *Poly Degra Stab*. 2007;92(7):1265–1278.
11. CaiJunqing, Wang Yiping, Zhou Limin, Huang Qunwu. Thermogravimetric analysis and kinetics of coal/plastic blends during co-pyrolysis in nitrogen atmosphere. *Fuel Proc Technol*. 2008;89:21–27.
12. Sharypov VI, Beregovtsova NG, Kuznetsov BN, Cebolla VL, Collura S, Finqueneisel G. Influence of reaction parameters on brown coal-polyolefinic plastic co-pyrolysis behavior. *J Anal Appl Pyrolysis*. 2007;78:257–264.
13. Regnier N, Guibe C. Methodology for multistage degradation of polyimide polymer. *Poly Degra Stab*. 1997;55:165–172.
14. Tomaszewicz E, Kotfica M. Mechanism and kinetics of thermal decomposition of Nickel(II) Sulfate(VI) hexahydrate. *J Therm Anal Calorim*. 2004;77(1):25–31
15. Coats AW, Redfern JP. Kinetic Parameters from the thermogravimetric data. *Nature*. 1964;201:68–69.
16. Doyle CD. Kinetic analysis of thermogravimetric data. *J Appl Poly Sci*. 1961;5(15):285–292.
17. Haruhiko Tanaka. Thermal analysis and kinetics of solid state reactions. *Thermochimica Acta*. 1995;267:29–44.
18. Hu Rongzu, Shi Qizhen. *Thermal analysis kinetics (in Chinese)*. Beijing. Science Press. 2001:47–184.
19. Huang Xiaofang, Wu Yulong, Yang Mingde, Hu Husheng, Dang Jie, Zhang Jianan. Mechanism and kinetics of thermal decomposition of bischofite. *Chinese J Proc Eng*. 2006;6(5):729–733.
20. Zheng Jilu, Zhu Xifeng, Guo Qingxiang, Zhu Qingshi. Thermal conversion of rice husks and sawdust to liquid fuel. *Waste Management*. 2006;26:1430–1435.

21. Gronli MG, Varhegyi G, Di Blasi C. Thermogravimetric analysis and devolatilization kinetics of wood. *Ind Eng Chem Res*. 2002;41: 4201–4208.
22. Gregg SJ, Sing KSW. *Adsorption, Surface Area and Porosity*. Academic Press, London; 1982.
23. Leofanti G, Padovan M, Tozzola G, Venturelli B. Surface area and pore texture of catalysts. *Catal Today*. 1998;41(1–3):207–219.
24. Mamleev V, Bourbigot S, Michel LeBras, Sophie Duquesne, Jaroslav Šesták. Modelling of nonisothermal kinetics in thermogravimetry. *Phys Chem Chem Phys*. 2000;20:4708–4716.
25. Órfão JJM, Antunes FJA, Figueiredo JL. Pyrolysis kinetics of lignocellulosic materials: three independent reactions model. *Fuel*. 1999; 78:349–358.
26. Cordero T, Rodríguez-Maroto JM, García F, Rodríguez JJ. Thermal decomposition of wood in oxidizing atmosphere. A kinetic study from non-isothermal TG experiments. *Thermochimica Acta*. 1991;191(1–22):161–178.
27. Zhong Shaoping. Study on the experiment of calcination reaction of calcium acetate and its mathematical simulation. Institute of Process Engineering, *Chinese Academy of Sciences*. 2002;7:57–59. Master Dissertation.
28. Chaudhuri N. Ray, Mrrra S, Pathak GK. Thermal investigations of the calcium salts of monocarboxylic aliphatic fatty acids. *J Therm Anal*. 1979;16:13–26.
29. Yue LH, Shui M, Xu Z. Decomposition kinetics of nanoparticle calcite (in Chinese). *Chinese J Inorg Chem*. 1999;15:225–229.
30. Liu JH, Zhang JY. Assessment of the apparent activation energies for gas/solid reactions-carbonate decomposition. *J Sci and Technol Beijing*. 2003;10(2):25–29.

Appendix A: Mathematical Derivation of Coats-Redfern and Doyle Equations

$$\int_0^{\alpha} \frac{d\alpha}{f(\alpha)} = F(\alpha) = \frac{A}{\beta}\int_0^T e^{-E/RT}dT \tag{A1}$$

Where $F(\alpha)$ is the integral function of conversion. The temperature integral $\int_0^T e^{-E/RT}dT$ on the righthand side of Eq. A1 has no exact analytical solution, but it can be approximated as follows

$$\begin{aligned}\int_0^T e^{-E/RT}dT &= \int_0^T (T)'\cdot e^{-E/RT}dT = Te^{-E/RT}\Big|_0^T \\ &\quad - \int_0^T T\cdot\left(e^{-E/RT}\right)'dT \\ &= Te^{-E/RT} - \int_{-\infty}^{T} T\cdot e^{-E/RT}\cdot\left(-\frac{E}{RT}\right)'dT \\ &= Te^{-E/RT} - \int_{-\infty}^{-\frac{E}{RT}} T\cdot e^{-E/RT}\cdot d\left(-\frac{E}{RT}\right) \\ &= \frac{E}{R}\cdot\frac{R}{E}\left[T\cdot e^{-E/RT} - \int_{-\infty}^{-\frac{E}{RT}} T\cdot e^{-E/RT}d\left(-\frac{E}{RT}\right)\right] \\ &= \frac{E}{R}\left[\frac{RT}{E}\cdot e^{-E/RT} - \int_{-\infty}^{-\frac{E}{RT}} \frac{RT}{E}e^{-E/RT}d\left(-\frac{E}{RT}\right)\right] \\ &= \frac{E}{R}\left[\frac{e^{-E/RT}}{E/RT} + \int_{-\infty}^{-\frac{E}{RT}} \frac{e^{-E/RT}}{E/RT}d\left(\frac{E}{RT}\right)\right]\end{aligned} \tag{A2}$$

In order to obtain the approximate formulas for temperature integral, let u is a polynomial vs. $\left(\frac{E}{RT}\right), dT = -\frac{E}{Ru^2}du$. Then Eq. A1 can be given by Eq. A3

$$F(\alpha) = \frac{A}{\beta}\int_0^T e^{-E/RT}dT = \frac{AE}{\beta R}\int_{\infty}^{u}\frac{-e^{-u}}{u^2}du = \frac{AE}{\beta R}P(u) \tag{A3}$$

where, $P(u) = \int_{\infty}^{u}\frac{-e^{-u}}{u^2}du$, the stepping integration expression of $P(u)$ can be derived as following

$$\begin{aligned}P(u) &= \int_{\infty}^{u}\frac{-e^{-u}}{u^2}du = \int_{\infty}^{u}\frac{1}{u^2}de^{-u} = \frac{e^{-u}}{u^2}\Big|_{\infty}^{u} - \int_{\infty}^{u}e^{-u}du^{-2} \\ &= \frac{e^{-u}}{u^2} - \int_{\infty}^{u}e^{-u}(-2)u^{-3}du = \frac{e^{-u}}{u^2} - \int_{\infty}^{u}2u^{-3}de^{-u} \\ &= \frac{e^{-u}}{u^2} - \frac{2e^{-u}}{u^3} + \int_{\infty}^{u}e^{-u}(-6)u^{-4}du \\ &= \frac{e^{-u}}{u^2} - \frac{2e^{-u}}{u^3} + \frac{6}{u^4}e^{-u}\Big|_{\infty}^{u} - \int_{\infty}^{u}e^{-u}d\frac{6}{u^4} \\ &= \frac{e^{-u}}{u^2} - \frac{2e^{-u}}{u^3} + \frac{6}{u^4}e^{-u} - \int_{\infty}^{u}\frac{24}{u^5}de^{-u} \\ &= \frac{e^{-u}}{u^2} - \frac{2e^{-u}}{u^3} + \frac{6}{u^4}e^{-u} - \frac{24}{u^5}e^{-u}\Big|_{\infty}^{u} + \int_{\infty}^{u}e^{-u}d\frac{24}{u^5} \\ &= \frac{e^{-u}}{u^2}\left(1 - \frac{2!}{u} + \frac{3!}{u^2} - \frac{4!}{u^3} + \cdots\right)\end{aligned} \tag{A4}$$

A combination of Eqs. A3 and A4 leads to

$$\int_0^T e^{-E/RT}dT = \frac{E}{R}\frac{e^{-u}}{u^2}\left(1 - \frac{2!}{u} + \frac{3!}{u} - \frac{4!}{u} + \cdots\right) \tag{A5}$$

The front two items of the right item of Eq. A5 are taking as the first-order approximate formular, the Coats-Redfern equation is obtained

$$\begin{aligned}\int_0^T e^{-E/RT}dT &= \frac{E}{R}\cdot P(u) = \frac{E}{R}\frac{e^{-u}}{u^2}\left(1 - \frac{2}{u}\right) = \frac{E}{R}e^{-u}\left(\frac{u-2}{u^3}\right) \\ &= \frac{RT^2}{E}\left(1 - \frac{2RT}{E}\right)e^{-E/RT}\end{aligned}$$

and

$$\ln\frac{F(\alpha)}{T^2} = \ln\frac{AR}{\beta E}\left(1 - \frac{2RT}{E}\right) - \frac{E}{RT}$$

Taking logarithm (base e) of the front two items of Eq. A4, we can obtain the following expression

$$\ln P(u) = -u + \ln(u-2) - 3\ln u(1-6) \tag{A6}$$

Using Doyle's approximation for In $P(u)$, if $20 \le u \le 60$, it is obvious that $-1 \le \frac{u-40}{20} \le 1$. The integral $P(u)$ can be expressed as

$$\begin{aligned}\ln P(u) &= -u - 3\ln 40 + \ln 38 + \left(1 + \frac{10}{19}\cdot\frac{u-40}{20}\right) \\ &\quad - 3\ln\left(1 + \frac{1}{2}\cdot\frac{u-20}{20}\right) \approx -5.3305 - 1.052u\end{aligned}$$

and

$$\ln F(\alpha) = \ln\frac{AE}{\beta R} - 5.3305 - 1.052\frac{E}{R}\cdot\frac{1}{T}$$

Appendix B. Fitting Results of Coats-Redfern Equation and Doyle Equation

No.	Symbol	Coats-Redfern Equation			Doyle Equation			Coats-Redfern Equation			Doyle Equation		
		E_a/J·mol^{-1}	A/min	r	E_a/J·mol^{-1}	A/min	r	E_a/J·mol^{-1}	A/min	r	E_a/J·mol^{-1}	A/min	r
		CA: the third temperature zone						CA: the fourth temperature zone					
1	D1	–	–	0.96998	–	–	0.97294	218790.10	1.88E+14	0.9993	214314.6	5.13E+13	0.99935
1	D1	259653.31	9.56E+21	0.9853	251578.3	1.46E+21	0.98586	263933.73	8.02E+16	0.99688	257277.7	1.52E+16	0.99705
2	D2	138946.79	6.81E+12	0.98856	136835.1	3.58E+12	0.98935	136889.81	6.50E+09	0.9985	136510.2	4.48E+09	0.99866
3	D3	275251.93	6.23E+22	0.98815	266406.3	8.48E+21	0.98857	274920.74	1.39E+17	0.99821	267722	2.44E+16	0.99831
4	D3	283612.50	2.83E+23	0.98942	274353.9	3.63E+22	0.98979	280784.53	3.11E+17	0.99869	273296.1	5.22E+16	0.99876
5	A1	95487.10	3.16E+09	0.99038	95522.41	3.46E+09	0.99133	141534.59	1.11E+10	0.9991	140925.5	7.18E+09	0.99919
6	A1.5	145730.48	2.12E+13	0.99071	143283.6	1.01E+13	0.99133	92118.11	1.86E+07	0.99905	93950.32	2.77E+07	0.99919
7	A2	70365.41	3.52E+07	0.99003	71641.81	6.97E+07	0.99133	67409.87	6.89E+05	0.99899	70462.74	1.87E+06	0.99919
8	A3	45243.72	3.42E+05	0.98927	47761.21	1.58E+06	0.99133	42701.63	2.21E+04	0.99887	46975.16	1.42E+05	0.99919
9	P1	127326.83	1.01E+12	0.98472	125789.2	6.31E+11	0.98586	128609.44	2.59E+09	0.99669	128638.9	2.02E+09	0.99705
10	P2	61163.59	7.16E+06	0.98344	62894.58	1.86E+07	0.98586	60947.30	3.15E+05	0.99626	64319.44	1.04E+06	0.99705
11	P3	39109.18	1.12E+05	0.98144	41929.72	6.82E+05	0.98586	38393.25	1.26E+04	0.99575	42879.62	9.90E+04	0.99705
12	P4	28081.97	1.26E+04	0.98035	31447.29	1.42E+05	0.98586	27116.23	2.25E+03	0.99514	32159.72	3.33E+04	0.99705
13	C1.5	–	–	0.92261	–	–	0.95419	–	–	0.68987	–	–	0.8783
14	C2	–	–	0.94142	–	–	0.95419	–	–	0.81323	–	–	0.8783
15	R2	136203.46	3.88E+12	0.98807	134227.3	2.12E+12	0.98891	134857.11	4.62E+09	0.99825	134577.9	3.28E+09	0.99844
16	R3	139306.42	5.77E+12	0.98903	137176.9	3.01E+12	0.98979	137034.84	5.26E+09	0.99861	136648	3.62E+09	0.99876
		CEB10: the second temperature zone						CEB10: the third temperature zone					
1	D1	27260.59	2.49E+04	0.98478	29576.97	2.46E+04	0.98879	–	–	0.97917	121444.3	5.83E+10	0.98091
2	D2	14041.01	8.83E+02	0.98865	17010.48	2.95E+03	0.99365	63924.52	4.24E+06	0.98401	65705.92	1.04E+07	0.98647
3	D3	30602.56	2.51E+04	0.99068	32753.84	1.99E+04	0.99299	129626.68	1.18E+11	0.98383	128162.2	7.36E+10	0.98513
4	D3	32459.27	4.24E+04	0.99303	34518.83	3.02E+04	0.99471	133427.23	2.37E+11	0.98595	131775	1.39E+11	0.98706
5	A1	15748.19	1.35E+03	0.9941	18633.33	3.66E+03	0.99659	67039.68	6.83E+06	0.98771	68667.17	1.53E+07	0.98954
6	A1.5	9214.29	2.31E+02	0.99193	12422.22	1.61E+03	0.99659	42961.06	1.11E+05	0.98662	45778.11	5.83E+05	0.98954
7	A2	5947.34	8.07E+01	0.9885	9316.663	1.16E+03	0.99659	30921.76	1.27E+04	0.9854	34333.59	1.24E+05	0.98954
8	A3	–	–	0.97278	6211.109	9.43E+02	0.99659	18882.45	1.24E+03	0.98242	22889.06	2.96E+04	0.98954
9	P1	–	–	0.97859	14788.49	2.39E+03	0.98879	–	–	0.9772	60722.14	5.74E+06	0.98091
10	P2	–	–	0.95022	7394.244	1.05E+03	0.98879	–	–	0.9724	30361.07	8.06E+04	0.98091
11	P3	–	–	0.82987	4929.496	9.55E+02	0.98879	–	–	0.96602	20240.71	2.31E+04	0.98091
12	P4	–	–	0.05099	3697.122	9.89E+02	0.98879	–	–	0.95736	15180.53	1.35E+04	0.98091
13	C1.5	–	–	0.49841	–	–	0.96551	–	–	0.75348	–	–	0.93566
14	C2	–	–	0.91168	–	–	0.96551	–	–	0.88574	–	–	0.93566
15	R2	13616.95	7.25E+02	0.98822	16607.37	2.55E+03	0.9935	62705.56	3.18E+06	0.98302	64547.18	8.10E+06	0.98566
16	R3	14302.88	7.59E+02	0.99056	17259.41	2.45E+03	0.99471	64115.54	3.49E+06	0.98471	65887.49	8.52E+06	0.98706
		CEB10: the fourth temperature zone						CEB12: the second temperature zone					
1	D1	224302.14	5.40E+14	0.9993	219546.2	1.40E+14	0.99936	37074.27	2.43E+05	0.9934	38876.29	1.34E+05	0.99483
2	D2	116194.29	4.41E+08	0.99802	116779.2	4.16E+08	0.99819	18760.39	2.99E+03	0.99574	21467.18	5.87E+03	0.99741
3	D3	234053.50	8.08E+14	0.99852	228815.8	1.93E+14	0.99859	39963.85	2.08E+05	0.99607	41623.12	9.89E+04	0.99629
4	D3	239248.84	1.66E+15	0.99789	233754.5	3.80E+14	0.99799	41518.32	3.18E+05	0.99717	43100.8	1.41E+05	0.99779
5	A1	120281.69	7.05E+08	0.99655	120664.7	6.21E+08	0.99685	20043.83	3.91E+03	0.99794	22687.21	6.80E+03	0.99878
6	A1.5	77969.80	2.80E+06	0.99638	80443.11	5.70E+06	0.99685	12088.40	5.26E+02	0.99727	15124.8	2.28E+03	0.99878
7	A2	56813.86	1.59E+05	0.99619	60332.33	5.95E+05	0.99685	8110.69	1.67E+02	0.99631	11343.6	1.43E+03	0.99878
8	A3	35657.92	7.82E+03	0.99578	40221.55	6.98E+04	0.99685	4132.98	4.02E+01	0.99272	7562.402	1.02E+03	0.99878
9	P1	108824.09	1.96E+08	0.99929	109773.1	2.10E+08	0.99936	16625.91	1.98E+03	0.99193	19438.15	4.86E+03	0.99483
10	P2	51085.06	7.94E+04	0.99922	54886.55	3.62E+05	0.99936	6401.73	1.03E+02	0.98419	9719.073	1.31E+03	0.99483
11	P3	31838.72	4.71E+03	0.99913	36591.03	5.17E+04	0.99936	–	–	0.96575	6479.382	1.01E+03	0.99483
12	P4	22215.55	1.01E+03	0.99902	27443.27	2.13E+04	0.99936	–	–	0.8984	4859.537	9.62E+02	0.99483
13	C1.5	–	–	0.59472	–	–	0.84937	–	–	0.15487	–	–	0.96075
14	C2	–	–	0.76205	–	–	0.84937	–	–	0.86828	–	–	0.96075
15	R2	114367.52	3.21E+08	0.99829	115042.7	3.12E+08	0.99844	18271.31	2.43E+03	0.99532	21002.26	5.02E+03	0.99717
16	R3	116297.44	3.55E+08	0.99879	116877.2	3.34E+08	0.99899	18847.94	2.43E+03	0.99633	21550.4	4.74E+03	0.99779

Appendix B. (Continued)

No.	Symbol	Coats-Redfern Equation			Doyle Equation			Coats-Redfern Equation			Doyle Equation		
		Ea/J·mol−1	*A*/min	*r*	Ea/J·mol−1	*A*/min	*r*	Ea/J·mol−1	*A*/min	*r*	Ea/J·mol−1	*A*/min	*r*
		CEB12: the third temperature zone						CEB12: the fourth temperature zone					
1	D1	–	–	0.96998	–	–	0.97294	218790.10	1.88E+14	0.9993	214314.6	5.13E+13	0.99935
2	D2	–	–	0.97663	65475.07	9.57E+06	0.98019	110751.87	1.75E+08	0.99979	111613.7	1.81E+08	0.99977
3	D3	–	–	0.97664	–	–	0.9785	224669.79	1.64E+14	0.99964	219903.8	4.26E+13	0.99967
4	D3	–	–	0.97973	131577.7	1.22E+11	0.98132	227712.20	2.51E+14	0.99976	222795.9	6.34E+13	0.99978
5	A1	67341.61	6.86E+06	0.98242	69011.88	1.54E+07	0.98501	112833.54	2.10E+08	0.99983	113592.6	2.10E+08	0.99987
6	A1.5	43142.13	1.11E+05	0.98089	46007.92	5.83E+05	0.98501	73001.54	1.22E+06	0.99984	75728.38	2.82E+06	0.99987
7	A2	–	–	0.97915	29508.8	1.98E+02	0.98501	53085.53	8.39E+04	0.99983	56796.28	3.56E+05	0.99987
8	A3	–	–	0.97496	18006.82	5.16E+01	0.98501	33169.53	4.96E+03	0.9998	37864.19	5.06E+04	0.99987
9	P1	–	–	0.96714	–	–	0.96714	106063.81	1.14E+08	0.99924	107157.3	1.28E+08	0.99935
10	P2	–	–	0.9602	–	–	0.96714	49700.67	5.96E+04	0.9991	53578.64	2.87E+05	0.99935
11	P3	–	–	0.951	–	–	0.96714	30912.95	3.85E+03	0.99893	35719.09	4.46E+04	0.99935
12	P4	–	–	0.93849	–	–	0.96714	21519.09	8.63E+02	0.99871	26789.32	1.92E+04	0.99935
13	C1.5	–	–	0.84532	–	–	0.9602	–	–	0.10936	–	–	0.9097
14	C2	–	–	0.9203	–	–	0.9602	–	–	0.75885	–	–	0.9097
15	R2	–	–	0.97548	–	–	0.97928	109390.09	1.36E+08	0.99875	110319.2	1.44E+08	0.9988
16	R3	–	–	0.97796	65788.83	7.99E+06	0.98132	110524.86	1.34E+08	0.99884	111397.9	1.40E+08	0.99886

Manuscript received Sept. 17, 2007, and revision received Mar. 7, 2008.